文章编号：1001-9014(2026)01-0090-07

DOI:10.11972/j.issn.1001-9014.2026.01.010

Bound states in the continuum for encoded imaging

HOU Shuai-Xing[1], YANG Si-Jia[2], SHEN Yun[1], DENG Xiao-Hua[2]

(1. Department of Physics, School of Physics and Materials Science, Nanchang University, Nanchang 330031, China;
2. Institute of Space Science and Technology, Nanchang University, Nanchang 330031, China)

Abstract: Metasurfaces are artificial structures that can finely control the characteristics of electromagnetic waves at subwavelength scales, and they are widely used to manipulate the propagation, phase, amplitude, and polarization of light. In this work, a bound state in the continuum (BIC) structure based on a metallic metasurface is proposed. By adjusting the metallic structure using CST and COMSOL software, a significant quasi-BIC peak can be achieved at a frequency of 0.8217 terahertz (THz). Through multi-level expansion analysis, it is found that the electric dipole (ED) is the main factor contributing to the resonant characteristics of the structure. By leveraging the characteristics of BIC, an imaging system was created and operated. According to the simulation results, the imaging system demonstrated excellent sensitivity and resolution, revealing the great potential of terahertz imaging. This research not only provides new ideas for the creation of BIC structures but also offers an effective reference for the development of high-performance terahertz imaging technology.

Key words: metasurface, bound states in the continuum, terahertz, multi-level expansion, imaging

用于编码成像的连续域束缚态

侯帅星[1], 杨思嘉[2], 沈 云[1], 邓晓华[2]

(1. 南昌大学 物理与材料科学学院 物理系,江西 南昌 330031;
2. 南昌大学 空间科学与技术研究院,江西 南昌 330031)

摘要:超表面是一种在亚波长尺度上精细调控电磁波特性的人工结构,广泛应用于操纵光的传播、相位、振幅和极化等特性。在这项工作中,提出了一种基于金属超表面的连续域束缚态(BIC)结构。通过使用CST和COMSOL两款软件对金属结构进行调整,能够在0.8217 THz的频率下实现显著的准BIC峰值。通过多级展开分析发现,电偶极子是该结构共振特性的主要因素。利用BIC的特性创建并运行了成像系统。根据仿真结果,该成像系统表现出了出色的灵敏度和分辨率,显示出太赫兹成像的巨大潜力。这项研究不仅为BIC结构的创建提供了新的想法,而且为高性能太赫兹成像技术的发展提供了有效的参考。

关 键 词:超表面;束缚态在连续体中;太赫兹;多级展开;成像

中图分类号:O439 **文献标识码**:A

Introduction

Terahertz waves occupy a specific frequency band between microwaves and infrared, with wavelengths ranging from 0.03 to 3 mm and frequencies from 0.1 to 10 THz [1-2]. Due to their unique physical characteristics, this frequency band plays an important role in scientific research and progress. Terahertz waves have a great potential for a wide range of applications because of their strong penetrating capability, non-ionizing nature, and minimal hazard to biological tissues.

Metasurfaces are typically composed of nano-antennas or resonators arranged in a periodic pattern. The geometric configurations, dimensions, and spatial arrangements of these elements can be specifically designed to produce particular electromagnetic responses [3-4]. By tun-

Received date: 2024-12-21, **revised date**: 2025-01-12 **收稿日期**:2024-12-21,**修回日期**:2025-01-12

Foundation items: Project supported by the National Natural Science Foundation of China (61927813, 61865009, 12104203), and Jiangxi Provincial Natural Science Foundation (20212ACB201007)

Biography: Hou Shuai-Xing, is currently working toward the Master degree in Physics with the Department of Physics, School of Physics and Materials Science, Nanchang University, Nanchang, China. His research interests include terahertz and meta-surface.

* **Corresponding author**: E-mail: sjyang@ncu.edu.cn

ing these parameters, one can achieve control over the local phase, amplitude, and polarization states of electromagnetic waves at the sub-wavelength scale, thereby enabling multifunctional and high-performance manipulation of electromagnetic waves. In recent years, metasurfaces have shown significant potential for applications across various fields. For example, in the field of optics, metasurfaces can be used to create super-lenses [5-7], that can break through the diffraction limit and achieve higher resolutions than conventional lenses. In the field of communications, metasurface technology can be employed to design efficient polarization converters [8, 9], thereby enhancing the efficiency and reliability of information transmission. Moreover, metasurfaces also demonstrate great potential in areas such as perfect absorption [10, 11], field enhancement [12], Polarization Control [13], and resonant coupling [14].

BIC was first introduced by von Neumann and Wigner in the context of quantum mechanics [15]. BIC refers to states that are confined within a continuous medium and do not radiate into the far field. The frequencies associated with these states are entirely located within the continuous spectrum, and they do not radiate energy into the far field [16]. Subsequently, this concept was rediscovered [17] and extended to other fields of wave physics, including acoustics [18] and optics [19, 20]. In practical applications , due to factors such as absorption, size [21], and other perturbations [22-23], BIC can be realized as a supercavity mode in the form of q-BIC when the Q factor and resonance width become finite under BIC conditions [24]. BIC have significant application scenarios in various fields. For example, in near-infrared photo detectors, high-Q resonances can enhance the interaction between light and quantum dots, thereby significantly improving light absorption and photoelectric conversion efficiency [25]. In the field of perfect absorbers, the symmetry-protected mechanism of toroidal dipole BICs maintains a highly stable resonant wavelength when adjusting the grating gap (with an experimental wavelength stability ratio of >15). This addresses the issue of wavelength drift and enhances the robustness and reliability of the device [26].

As an emerging field in electromagnetic wave control technology, coding metasurfaces have demonstrated great potential in imaging and sensing applications in recent studies. Unlike traditional reflective surfaces and lenses, coding metasurfaces utilize their small and highly tunable structural units to achieve precise control over electromagnetic waves [27]. This capability can be widely applied in various fields, including imaging [28-34], beam splitting [35], and vortex beam generation [36-41].

Traditional imaging systems still have limitations in beam control and imaging resolution. However, coded metasurfaces can achieve highly customized manipulation of electromagnetic waves through the meticulous design of their micro-structural units. This paper first provides an overview of the design methods for q-BIC structures and the fundamental principles of coded metasurfaces. It elaborates on how desired frequency response characteristics can be achieved through the careful arrangement and optimization of unit parameters, while also discussing the importance of multi-level expansion in the establishment of q-BICs. It is worth noting that by altering the structure to generate q-BIC peaks, the transmission efficiency at specific frequencies is significantly enhanced, thereby greatly improving the performance of imaging systems. Finally, the paper explores the potential challenges that BIC imaging may face in practical applications and looks forward to future development directions. Through comprehensive discussions and experimental validation, this study aims to elucidate the potential of q-BIC structured coded metasurfaces in the field of electromagnetic imaging technology.

1 Principle and design

The schematic diagram of the BIC metasurface we designed is shown in Figure 1. The device is composed of butterfly-shaped metallic structures arranged periodically, which are fabricated on a polyimide (PI) film substrate. Each individual structure consists of two semi-elliptical metallic patches and a central metallic strip, forming a horizontally symmetrical configuration. The central strip is designed to be movable in the vertical direction, with a displacement of h = 20 μm. The gap between structures is denoted as g = 20 μm, while the overall periodicity of the structure is P = 150 μm. The width (w) of the metallic structure is 10 μm, and its length (l) is 120 μm. The radii of the elliptical metallic patches are a_1 = 40 μm and a_2 = 20 μm, respectively. The relative permittivity of the PI film used is 3.5, and copper is employed as the metallic material in the device structure. The incident electric field ($\boldsymbol{E}$) is oriented along the x-axis, and the wave vector ($\boldsymbol{k}$) is aligned along the negative z-axis. The vertical displacement of the central metallic strip transforms the BIC into a q-BIC state. To optimize the structure and conduct a comprehensive analysis of the electromagnetic field characteristics, we mainly use the simulation software COMSOL and CST. In our simulations, periodic boundary conditions are applied in the x and y directions, while the z direction is treated with a Perfectly Matched Layer (PML).

2 Simulation and conclusion

The resonance peaks originate from the variation in the position of the intermediate metal strip. The vertical displacement of the metal strip induces a transition from BIC to q-BIC. This transition allows a portion of the local field energy to leak out, thereby transforming the bound state with an infinitely large Q factor into a quasi-bound state (q-BIC) with a finite Q factor. To explicitly investigate the influence of structural variation on the transmission spectrum, a position variation parameter, denoted as h, was introduced. When the value of h is zero, the transmission spectrum exhibited no significant peaks. In contrast, when h is increased to 20 μm, a distinct transmission peak emerges in the spectrum, as shown in Figure 2.

As the parameter h varies from -25 μm to 25 μm, a

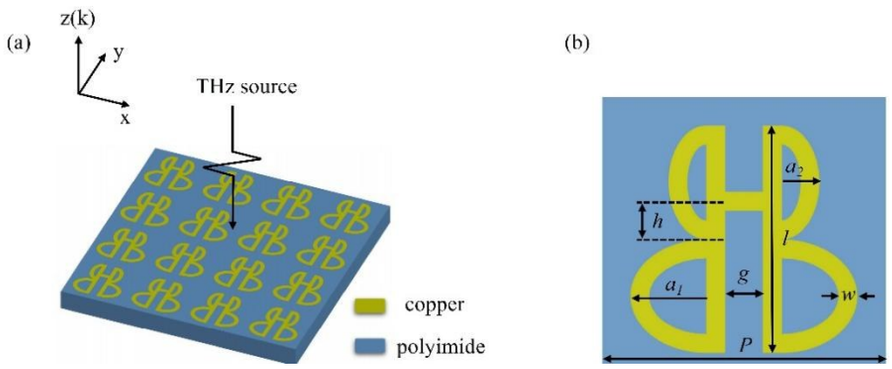

Fig. 1 Designed metallic metasurface: (a) displays the overall appearance of the design, while (b) provides a detailed schematic diagram of the unit structure for a clearer understanding of its construction and functionality.
图1 设计金属超表面:(a)展示设计整体外观;(b)提供单元结构的详细示意图,以便更清晰地理解其构造与功能。

significant shift in the resonance peak occurs, accompanied by a gradual increase in both the resonance linewidth and modulation depth, as depicted in Figure 3. This phenomenon indicates that the variation in the position of the intermediate metal strip leads to enhanced resonant radiation, which in turn results in energy leakage. Figure 4 presents the relationship between the Q factor and the relevant parameters, with Q defined as follows:

$$Q = \frac{f_0}{FWHM} \quad , \quad (1)$$

In this context, the FWHM refers to the half-width at half-maximum of the resonance peak. Since the bound states in the continuum do not interact with free space, radiation leakage is prevented. As a result, the FWHM is effectively zero, and the Q factor tends toward infinity. However, when the structure of the metasurface is perturbed, the BIC transitions into a q-BIC mode, thereby inducing resonance [42]. By leveraging structural modifications to control the BIC, it is possible to manipulate the degree of radiation leakage as well as the magnitude of the Q factor.

In addition, we have conducted an in-depth analysis of the structure using the multipole decomposition method. The scattering properties of nanoparticles can be thoroughly examined through this method, where the far-field scattering energy generated by each multipole at the resonance point can not only be visualized but also precisely quantified. Various types of electromagnetic sources, such as electric quadrupoles, toroidal dipoles, and magnetic quadrupoles, exhibit distinct differences in

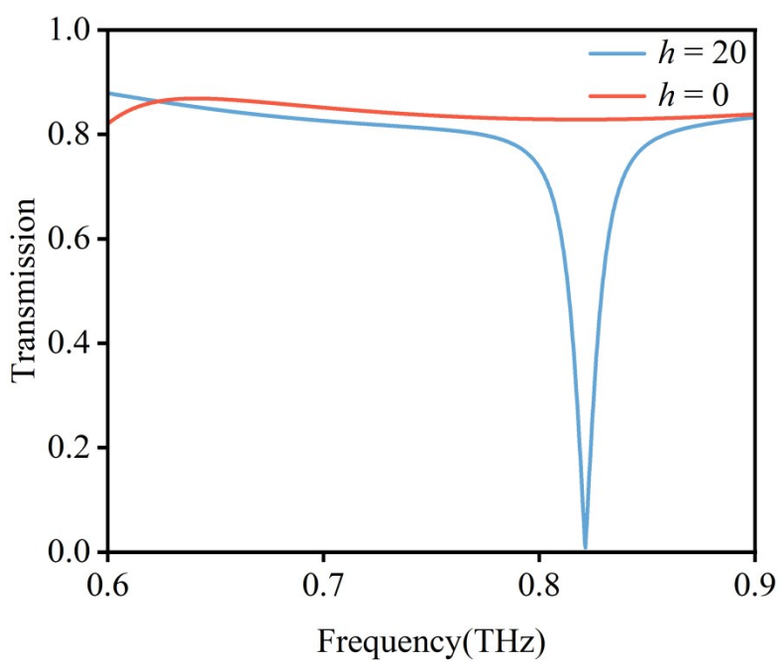

Fig. 2 The transmission spectrum as a function of frequency when the metal strip is not displaced (h = 0 μm, in red). The transmission spectrum as a function of frequency when the metal strip is displaced (h = 20 μm, in blue).
图2 金属条未位移时(h = 0 μm,红色)的透射光谱随频率变化曲线。金属条位移时(h = 20 μm,蓝色)的透射光谱随频率变化曲线。

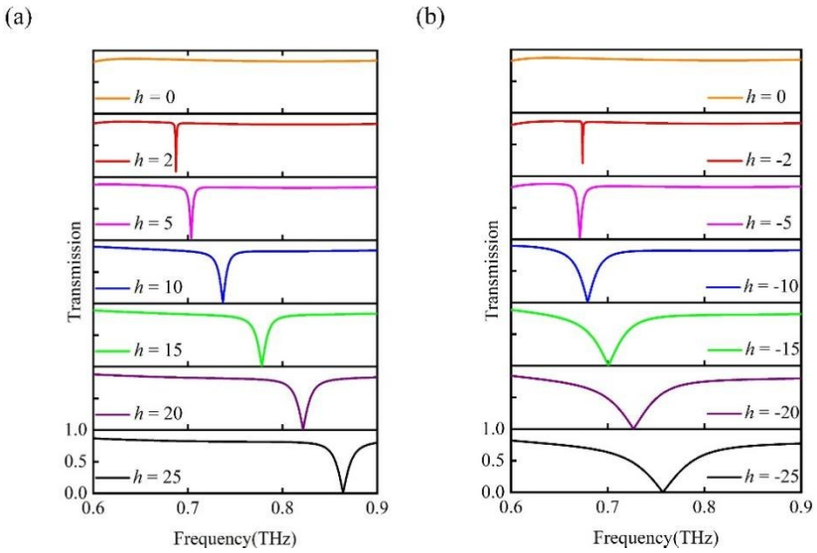

Fig. 3 （a）Simulated results for the transmission rate *h* ranging from 0 μm to 25 μm;（b）Simulated results for the transmission rate *h* ranging from 0 μm to -25 μm.
图3 （a）传输率h在0 μm至25 μm范围内的模拟结果;（b）传输率h在0 μm至-25 μm范围内的模拟结果。

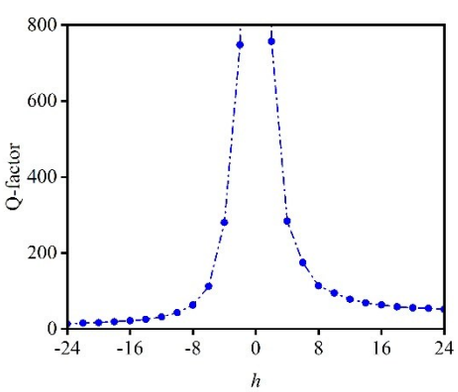

Fig. 4 The relationship between the Q factor and the variation of the *h* parameter.
图4 Q因子与h参数变化之间的关系。

their radiation field distributions. At the resonant frequency, the distribution of the electromagnetic field is primarily influenced by the multipole with the highest scattering energy. The characteristics of the multipole moments for different multipoles are articulated within the Cartesian coordinate system as follows [43].

$$P = \frac{1}{i\omega}\int j d^3 r \quad . \quad (2)$$

$$M = \frac{1}{2c}\int (r \times j) d^3 r \quad . \quad (3)$$

$$Q_{\alpha\beta}^{(e)} = \frac{1}{2i\omega}\int \left[\left(r_\alpha j_\beta + r_\beta j_\alpha \right) - \frac{2}{3}\left(r \cdot j \right)\delta_{\alpha\beta} \right] d^3 r \quad . \quad (4)$$

$$Q_{\alpha\beta}^{(m)} = \frac{1}{3c}\int \left[\left(r \times j \right)_\alpha r_\beta + \left(r \times j \right)_\beta r_\alpha \right] d^3 r \quad . \quad (5)$$

$$T = \frac{1}{10c}\int \left[\left(r \cdot j \right) r - 2 r^2 j \right] d^3 r \quad . \quad (6)$$

Equation（2）through（6）delineate the properties of the ED, Magnetic Dipole（MD）, Electric Quadrupole（EQ）, Magnetic Quadrupole（MQ）, and Toroidal Dipole（TD）. In these equations, the variable *r* signifies the position vector, *c* represents the speed of light, ω denotes the angular frequency of light, while α and β are the parameters associated with the x and y directions, respectively. Additionally, *j* indicates the displacement current density. By analyzing the electromagnetic field and refractive index distribution obtained from simulation results, it is possible to compute the normal radiation power of various dipole types in accordance with Equation（7）.

$$I = \frac{2\omega^4}{3c^3}|P|^2 + \frac{2\omega^4}{3c^3}|M|^2 + \frac{\omega^6}{5c^5}\left|Q_{\alpha\beta}^{(e)}\right|^2 + \frac{\omega^6}{20c^5}\left|Q_{\alpha\beta}^{(m)}\right|^2 + \frac{2\omega^6}{3c^5}|T|^2 \quad . \quad (7)$$

The far-field radiation power, as determined by the previously mentioned equations, is illustrated in Figure 5. The figure clearly indicates that at the resonance frequency, the radiation contribution from the ED mode is markedly greater than that of the other modes, which are substantially suppressed.

As shown by the positive and negative variations of the h value in Figure 4, we can observe that the magnitude of the changes in the Q value is not consistent. The reason for this phenomenon is the difference in the major axis dimensions of the upper and lower semi-ellipses. Next, we will conduct an in-depth investigation into the impact of changes in the major axis dimensions on the Q value. To this end, we keep the major axis length of the lower semi-ellipse, denoted as a_1, fixed at 40 μm, while controlling *h* at 6 μm, and then vary the major axis length of the upper semi-ellipse, referred to as a_2. Figure 6 illustrates the trend of the Q value as a function of a_2, showing that the Q value gradually decreases as a_2 increases.

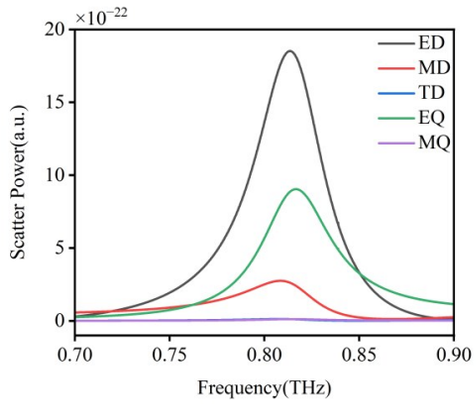

Fig. 5 The multipole expansion of the scattering patterns
图5 散射模式的多极展开。

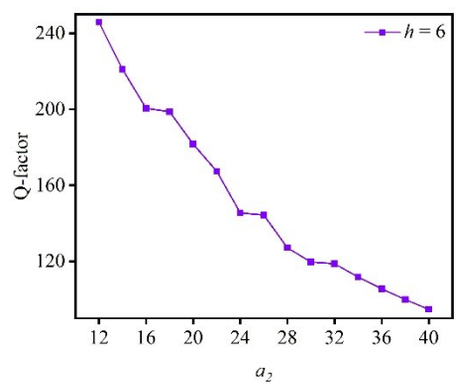

Fig. 6 The change in the Q factor with respect to a_2 when h is set to 6 μm.
图6 当h的值设为6 μm时,Q因子随a2的变化关系。

Figure 7 presents the distribution of the electric field, magnetic field, and surface current on the metasurface at a frequency of 0.8217 THz, with h values set at 20 μm and 0 μm, respectively. This analysis further substantiates the perturbation of BIC and the impact of structural disruption on the excitation mechanisms. When terahertz waves interact with the metallic structure, the surface plasmon effect causes electrons on the metal surface to resonate at the same frequency as the incident wave, resulting in an intensified electromagnetic field localized within a confined area on the metal surface [44]. At a h value of 0 μm, the energy emitted by the x-polarized wave on the metasurface exhibits no significant up-down asymmetry, leading to a locally excited electromagnetic field that is mirror-symmetric about the x-axis (refer to Figures 7(d) and (e)). As the connecting component is displaced, the electric and magnetic fields correspondingly shift, indicating that the structural change leads to radiation leakage and modifies the radiative field (see Figures 7(a) and (b)). The distribution trend of the generated surface current is illustrated in Figure 7(f), revealing the distribution of surface current in the upper and lower regions. Following the structural change, the surface current undergoes a redistribution, as shown in Figure 7(c), which significantly differs from the previous distribution and serves as a critical condition for the emergence of new transmission peaks [45].

Figure 8 displays a color map depicting the variations in transmission characteristics and resonant responses across a range of structural parameters. This figure illustrates the transition from a BIC characterized by an infinite Q factor to a q-BIC state with a finite yet high Q factor. In this context, the parameter h is used to adjust the structural changes within the system. Additionally, the figure reveals that the transition trends of the BIC on the left and right sides exhibit notable differences,

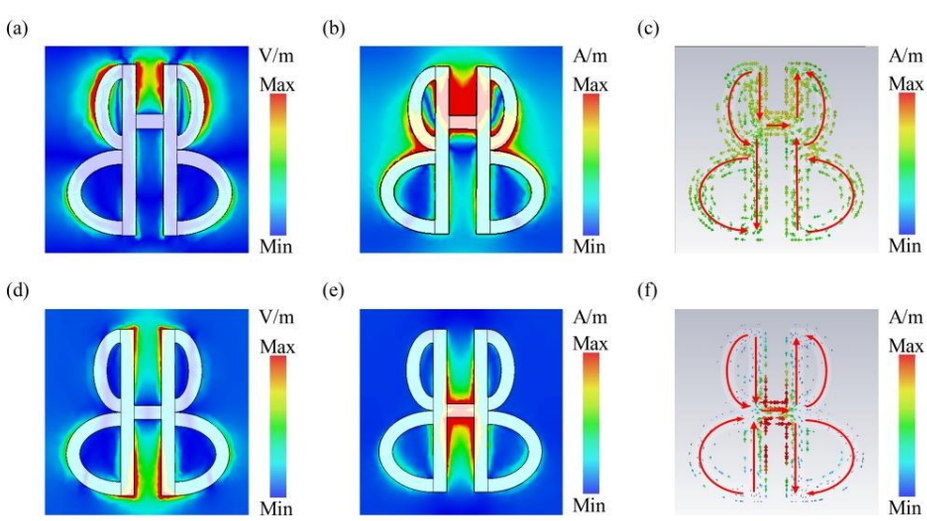

Fig. 7 When h = 20 μm and f = 0.8217 THz, it illustrates the distribution of (a) the electric field, (b) the magnetic field, and (c) the surface current trend. When h = 0 μm and f = 0.8217 THz, it illustrates the distribution of (d) the electric field, (e) the magnetic field, and (f) the surface current trend.
图7 当h = 20 μm且f = 0.8217 THz时,展示了(a)电场分布、(b)磁场分布以及(c)表面电流趋势。当h = 0 μm且f = 0.8217 THz时,图示展示了(d)电场分布、(e)磁场分布以及(f)表面电流趋势。

which can be attributed to the distinct upper and lower radii of the ellipse, denoted as a_1 and a_2, respectively.

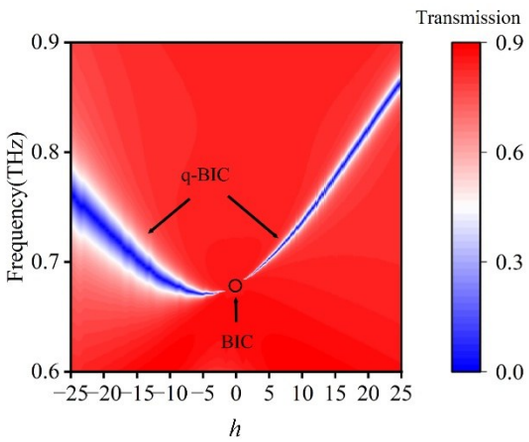

Fig. 8　The color-simulated transmission spectra for different *h*.
图8　不同h值的颜色模拟透射光谱。

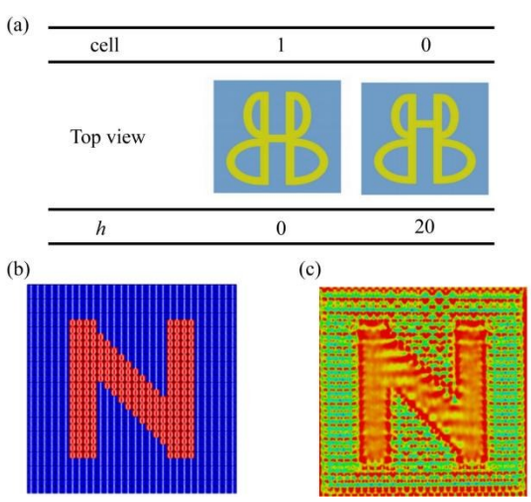

Fig. 9　(a) presents the smallest unit of encoding; (b) The sorting of the encoding; (c) represents the final image obtained from the simulation.
图9(a)　展示了编码的最小单元;(b)呈现编码的排序过程;(c)则代表模拟所得的最终图像。

In this study, we first used MATLAB coding to establish a simulation model in CST as shown in Figure 9 (b), then added a plane wave incident in the form of x-polarization, and added a field monitor for the 0.8217 THz frequency band. Specifically, we selected a metasurface composed of binary "1" and "0" cells to effectively demonstrate imaging effects. The complete encoding array is structured as a 30×30 grid. Under the illumination of the incident light, the "1" cells exhibit a transmission amplitude of 0.83 for the incoming light, while the "0" cells display a significantly lower transmission amplitude of only 0.01. As a result, a clear image is observed through the field monitor as shown in Figure 9(c), which is not present at other frequencies. This research provides valuable insights into the controllability of near-field imaging associated with BIC on the metasurface.

3　Discussion

Our task commences with an extensive examination of metasurface technology and its applications in the manipulation of electromagnetic waves, particularly highlighting its considerable potential within the terahertz frequency spectrum. Terahertz waves, due to their distinctive physical characteristics, exhibit extensive applicability across various domains, including imaging and sensing. The BIC structure introduced in this study exemplifies an innovative design methodology that utilizes the sub-wavelength properties of metasurfaces to facilitate precise control over electromagnetic waves. This research offers significant contributions to the academic discourse surrounding metasurface and terahertz technologies. The design and implementation of the BIC structure not only illustrate the capabilities of metasurface technology in electromagnetic wave manipulation but also open new pathways for advancements in imaging and sensing applications. Future investigations are anticipated to delve deeper into the optimization techniques for BIC structures and their practical applications, while simultaneously addressing existing technological challenges. This article serves as a valuable resource and source of inspiration for scholars in related disciplines and is expected to foster the application and progression of terahertz technology across a wider array of fields.

Acknowledgment

Project supported by the National Natural Science Foundation of China (Grant Nos. 61927813, 61865009 and 12104203), and Jiangxi Provincial Natural Science Foundation (No. 20212ACB201007).

References

[1] Houtong Chen, Antoinette J Taylor, Nanfang Yu. A review of metasurfaces: physics and applications.[J] Reports on Progress in Physics, 2016, 79: 076401.
[2] Xiaofei Zang, Bingshuang Yao, Lin Chen, et al. Metasurfaces for manipulating terahertz waves.[J] Light: Advanced Manufacturing, 2021, 2: 148-172.
[3] Viktor G. Veselago. The electrodynamics of substances with simultaneously negative values of ε and μ.[J] Soviet Physics Uspekhi, 1968, 10: 509-514.
[4] Alexander V. Kildishev, Alexandra Boltasseva, Vladimir M. Shalaev. Planar Photonics with Metasurfaces.[J] Science, 2013, 339: 1232009.
[5] Ho-Seok Ee, Ritesh Agarwal. Tunable Metasurface and Flat Optical Zoom Lens on a Stretchable Substrate.[J] Nano Letters, 2016, 16: 2818-2823.
[6] Dan Hu, Xinke Wang, Shengfei Feng, et al. Ultrathin Terahertz Planar Elements.[J] Advance Optical Material, 2013, 186 - 191.
[7] Jingwen He, Jiasheng Ye, Xinke Wang, et al. A broadband terahertz ultrathin multi-focus lens.[J] Scientific Reports, 2016, 6: 28800.
[8] Zhengyong Song and Jiahe Zhang. Achieving broadband absorption and polarization conversion with a vanadium dioxide metasurface in the same terahertz frequencies.[J] Optics Express, 2020, 28: 12487-12497.
[9] Min Jia, Zhuo Wang, Heting Li, et al. Efficient manipulations of circularly polarized terahertz waves with transmissive metasurfaces.[J] Light: Science & Applications, 2019, 8: 16.
[10] Grant J, McCrindle I. J. H, Li C, et al. Multispectral metamaterial absorber.[J] Optics Letters, 2014, 39(5): 1227-1230.
[11] Benxin Wang, Guizhen Wang, Weiqing Huang. Single Metamaterial

Resonator Having Five-Band Terahertz Near-Perfect Absorption.[J] IEEE Photonics Technology Letters, 2017, 29(21): 1888-1891.
[12] Cao B, Quan K, Chen B, et al. Towards Ultra-strong Terahertz Field Enhancement in Nanogap Split Ring Resonators. [C] The 9th International Symposium on Ultrafast Phenomena and Terahertz Waves, OSA Technical Digest (online) (Optica Publishing Group, 2018), paper WI12.
[13] Jin Chen, Feilong Yu, Xingsi Liu, et al. Polychromatic full-polarization control in mid-infrared light.[J] Light: Science & Applications, 2023, 12(1): 1-14.
[14] Jan Wallauer, Christian Grumber, Markus Walther. Mapping the coupling between a photo-induced local dipole and the eigenmodes of a terahertz metamaterial. [J] Optics Letters, 2014, 39(21): 6138-6141.
[15] J. von Neumann, E.P.Wigner. Über merkwürdige diskrete eigenwerte. [M] Springer, 1993, pp 291 - 293.
[16] Chia Wei Hsu, Bo Zhen, A. Douglas Stone, et al. Bound States in the Continuum.[J] Nature Reviews Materials, 2016, 1(9):16048.
[17] H. Friedrich, D. Wintgen. Interfering resonances and bound states in the continuum.[J] Phys. Rev. A, 1985, 32(6): 3231-3242.
[18] R. Parker. Resonance effects in wake shedding from parallel plates: some experimental observations. [J] Sound Vibr, 1966, 4(1): 62-72.
[19] D. C. Marinica, A. G. Borisov. Bound states in the continuum in photonics.[J] Physical Review Letters, 2008, 100: 183902.
[20] Evgeny N. Bulgakov, Almas F. Sadree. Bound states in the continuum in photonic waveguides inspired by defects.[J] Physical Review B, 2008, 78: 075105.
[21] Z. F. Sadrieva, M. A. Belyakov, M. A. Balezin, et al. Experimental observation of symmetry protected bound state in the continuum in a chain of dielectric disks.[J] Physical Review A, 2019, 99: 053804.
[22] Zarina F. Sadrieva, Ivan S. Sinev, Kirill L. Koshelev, et al. Transition from optical bound states in the continuum to leaky resonances: Role of substrate and roughness. [J] ACS Photonics, 2017, 4: 723-727.
[23] Chaobiao Zhou, Lujun Huang, Rong Jin, et al. Bound States in the Continuum in Asymmetric Dielectric Metasurfaces.[J] Laser Photonics Rev. 2023, 17: 2200564.
[24] Mikhail Rybin, Yuri Kivshar. Supercavity lasing.[J] Nature, 2017, 541: 164-165.
[25] Jiaoyang Guo, Rong Jin, Zhenchu Fu, et al. Topologically Engineered High-Q Quasi-BIC Metasurfaces for Enhanced Near-Infrared Emission in PbS Quantum Dots.[J] Nano Lett. 2025, 25: 2357-2365.
[26] Rong Jin, Lujun Huang, Chaobiao Zhou, et al. Toroidal Dipole BIC-Driven Highly Robust Perfect Absorption with a Graphene-Loaded Metasurface.[J] Nano Lett. 2023, 23: 9105-9113.
[27] Tie Jun Cu, Mei Qing Qi, Xiang Wan, et al. Coding metamaterials, digital metamaterials and programmable metamaterials.[J] Light-Sci Appl, 2014, 3: e218.
[28] Jingxiang Gao, Hang Liu, Man Zhang, et al. Dynamic switching between bound states in the continuum (BIC) and quasi-BIC based on a Dirac semimetal terahertz metasurface.[J] Chem. Phys, 2022, 24(46): 25571 - 25579.
[29] Jitao L, Jie Li, Chenglong Zheng, et al. Dynamic control of reflective chiral terahertz metasurface with a new application developing in full grayscale near-field imaging.[J] Carbon, 2021, 172: 189-199.
[30] Rou-Lan Wu, Jiu-Sheng Li. Circular/linear dichroism and anisotropy based on tunable terahertz metasurfaces.[J] Journal of Computational Electronics, 2024, 23: 348-357.
[31] Yaowei Dai, Cong Chen, Peng Gao, et al. 3-bit reconfigurable THz metasurface based on structured light illumination for vortex beams and holographic imaging. [J] Optics & Laser Technology, 2024, 169: 109951.
[32] Xiaoyuan Hao, Yupeng Chen, Mai Liu, et al. Recent Advances in Terahertz Manipulations Using C-Shape-Split-Ring-Resonator Metasurfaces.[J] Advanced Optical Materials, 2024, 12: 2302975.
[33] Dongliang Xie, Luzhen Chen, Tao Luo, et al. Phase distribution and circular dichroism switchable terahertz chiral metasurface.[J] Optics Express, 2024, 32(7): 12104-12117.
[34] Zhenkai Li, Chunyang Jian, Kun Wang, et al. Active manipulation of Dirac semimetals supported chiral coding metasurfaces for multifunctional applications in terahertz region. [J] Results in Physics, 2023, 46: 106323.
[35] Shuo Liu, Tie Jun Cui, Lei Zhan, et al. Convolution Operations on Coding Metasurface to Reach Flexible and Continuous Controls of Terahertz Beams.[J] Advanced Science, 2016, 3(10): 1600156.
[36] Hammad Ahmed, Yuttana Intaravanne, Yang Ming, et al. Multichannel Superposition of Grafted Perfect Vortex Beams. [J] Advanced Materials, 2022, 34(30): 2203044.
[37] Bin He, Jiaqi Liu, Yongzhi Cheng, et al. Broadband and thermally switchable reflective metasurface based on Z-shape InSb for terahertz vortex beam generation.[J] Physica E: Low-dimensional Systems and Nanostructures, 2022, 144: 115373.
[38] L Jiaqi Liu, Yongzhi Cheng, Fu Chen, et al. High-efficiency reflective metasurfaces for terahertz vortex wave generation based on completely independent geometric phase modulations at three frequencies. [J] Journal of the Optical Society of America B, 2022, 39: 1752-1761.
[39] Wanying Liu, Quanlong Yang, Quan Xu, et al. Multichannel terahertz quasi-perfect vortex beams generation enabled by multifunctional metasurfaces. [J] Nanophotonics, 2022, 11(16): 3631 - 3640.
[40] B. A. Knyazev, Yu. Yu. Choporova, M. S. Mitkov, et al. Generation of Terahertz Surface Plasmon Polaritons Using Nondiffractive Bessel Beams with Orbital Angular Momentum.[J] Physical Review Letters, 2015, 115(16): 163901.
[41] Nanfang Yu, Patrice Genevet, Mikhail A. Kats, et al. Light Propagation with Phase Discontinuities: Generalized Laws of Reflection and Refraction.[J] Science, 2011, 334: 333-337.
[42] Lujun Huang, Rong Jin, Chaobiao Zhou, et al. Ultrahigh-Q guided mode resonances in an All-dielectric metasurface.[J] Nature Communications 2023, 14: 3433.
[43] V. Savinov, V. A. Fedotov, N. I. Zheludev, et al. Toroidal dipolar excitation and macroscopic electromagnetic properties of metamaterials. [J] Phys Rev B, 2014, 89: 205112.
[44] R. H. Ritchie, E. T. Arakawa, J. J. Cowan, et al. Surface-plasmon resonance effect in grating diffraction. [J] Phys. Rev. Lett, 1968, 21: 1530 - 1533.
[45] Kirill Koshelev, Gael Favraud, Andrey Bogdanov, et al. Nonradiating photonics with resonant dielectric nanostructures. [J] Nanophotonics, 2019, 8(5): 725 - 745.